JOURNAL OF GUIDANCE, CONTROL, AND DYNAMICS
Vol. 18, No. 6, November–December 1995

Passive Airborne Navigation and Terrain Avoidance Using Gravity Gradiometry

David M. Gleason*
Phillips Laboratory, Hanscom Air Force Base, Massachusetts 01731-3010

The Air Force is studying the integration of an inertial navigation system (INS) and a gravity gradiometer for passive, purely autonomous navigation and terrain avoidance. In such an inertial/gradiometric system, navigation errors are bounded by passive updates consisting of real-time matches between the single flight-path profile of measured gravity gradients and stored, constant-altitude grids of estimated gradients based on all available ground gravity, terrain elevation, and mass density data. An envisioned mechanization is block diagrammed and reviewed. The relationship between the system's three-dimensional position errors, the self-generated errors of the INS and gradiometer, and the errors in the stored gradient grids is discussed. If high-resolution grids of ground gravity and terrain elevation data exist for the fly-over area, then airborne grids of gravity gradients can be rigorously estimated without any assumption involving terrain mass densities. If ground gravity data is lacking, a nominal terrain density value is assumed and terrain-implied grids of gradients can be nonoptimally estimated. The two estimation techniques possess no relative bias and produce airborne grids having similar gradient trends and statistical properties. The power spectrum densities of local terrain-implied gravity fields are shown to dominate those of local geology-implied (subterranean) fields along the shorter wavelengths where most of the spectral sensitivities of the gradiometer's signal reside. The effects of aboveground altitudes, aircraft velocities, and low-noise gradient production rates on terrain feature resolvability are discussed. The performance specifications of gradiometers currently being developed are reviewed. Although the requirements of this application are demanding, it is felt they can be engineered into an optimal 21st century gravity gradiometer design.

Nomenclature

G = gravitational constant
H = maximum terrain elevation
$\boldsymbol{H}$ = measurement matrix
h_d = constant altitude of the current grid estimations
h_0 = lowest operational altitude involved
ε = errors in stored gradient estimates

I. Basic Signal Processing and Gravity Gradient Matching Mechanizations

A GRAVITY gradiometer is essentially an elaborate array of accelerometers positioned such that by suitably taking combinations of accelerometer differences one cancels out common linear platform (nongravity) accelerations. One is, thus, left sensing gradients of gravity along the baselines of accelerometer pairs. By contrast, a single accelerometer (gravimeter) can not separate the platform accelerations from the gravitational pull present. The ultimate measurements of a full tensor gradiometer are the five second-order, independent gradients of the actual gravity field that make up the full, symmetric, zero-trace, gradient tensor. This nine-element tensor is initially measured in some designated sensor coordinate frame and then transformed to the local (north, east, down) navigation frame. If W denotes the Earth's actual gravitational potential (in m^2/s^2 potential units), then the six unique navigation-frame, second-order, gravity gradient tensor elements are denoted by W_{NN}, W_{EE}, W_{DD}, W_{NE}, W_{ND}, and W_{ED} where, e.g., $W_{ND} = \partial^2 W/\partial N \partial D$, and the gradients are typically expressed in $10^{-9}/s^2$ Eotvos units.

Gravity gradient disturbance values, denoted, e.g., by T_{ND}, are obtained by removing the so-called normal gradients implied by a homogeneously dense reference ellipsoid that approximates the Earth in size and shape. The gradiometer's ability to sense gravitational forces on a moving platform make it an ideal candidate to perform the real-time gravity compensation required for purely autonomous navigation, attainable with a self-inclusive inertial/gradiometric navigation system (possibly supplemented by barometric altimeters and/or startrackers). A more detailed description of a gravity gradiometer design is given in Sec. V.

As presented in Affleck and Jircitano,[1] the envisioned navigation system would consist of an inertial navigation system (INS) passively updated with position fixes by real-time matching the flight-path profile of measured T_{ij} gradient disturbances with stored grids of estimated T_{ij} based on all available geophysical data. The part of the Kalman filter's external observation model related to the gradient matching, at each t_k updating epoch, takes on the well-known form

$$\delta \boldsymbol{L} = \boldsymbol{L}^{\text{measured}}(t_k) - \boldsymbol{L}^{\text{stored}}(t_k) = [\boldsymbol{H}(t_k)] \cdot \boldsymbol{x}(t_k) + \boldsymbol{\varepsilon}^{\text{stored}}(t_k) \quad (1)$$

where $\boldsymbol{x}$ is the overall system error state vector containing the navigation-frame $\delta \boldsymbol{R}$ position, $\delta \dot{\boldsymbol{R}}$ velocity, and $\delta \boldsymbol{\psi}$ orientation error states, and self-generated instrument-frame $\delta \boldsymbol{I}$ INS and $\delta(\mathbf{gg})$ gravity gradiometer error sources (includes biases, scale factor errors, misalignments, etc., all of which contain correlated and white noise components). In particular, each scalar T_{ij} second-order, navigation-frame gradient difference is given by

$$T_{ij}^{\text{measured}} - T_{ij}^{\text{stored}} = -\left(T_{ij\,\text{rate-changes w.r.t.}(N,E,D)}^{\text{stored}}\right)^T \cdot \delta \boldsymbol{R} + \varepsilon_{T_{ij}}^{\text{stored}} + \delta(\mathbf{gg})_{T_{ij}}^{\text{measured}} \quad (2)$$

where the T_{ij} rate changes come from the third-order gradient tensor related to the stored data and it is assumed the $[C_{\text{gradiometer instrument frame}}^{\text{to nav frame}}]$ transformation matrix was applied to the two measured terms in Eq. (2).

Such updating is clearly nonemanating and nonjammable. Figure 1 contains proposed signal processing and gradient matching block diagrams given by Affleck and Jircitano.[1] Additional updating by onboard barometric altimeters is assumed, which of course will increase the number or rows in the comprehensive $[\boldsymbol{H}]$, $\delta \boldsymbol{L}$, and $\boldsymbol{\varepsilon}$. Given the INS's current latitude, longitude, and altitude estimates, the Kalman filter optimally matches the two gradient

Received Oct. 21, 1994; revision received April 19, 1995; accepted for publication April 21, 1995.

*Geophysics Directorate.

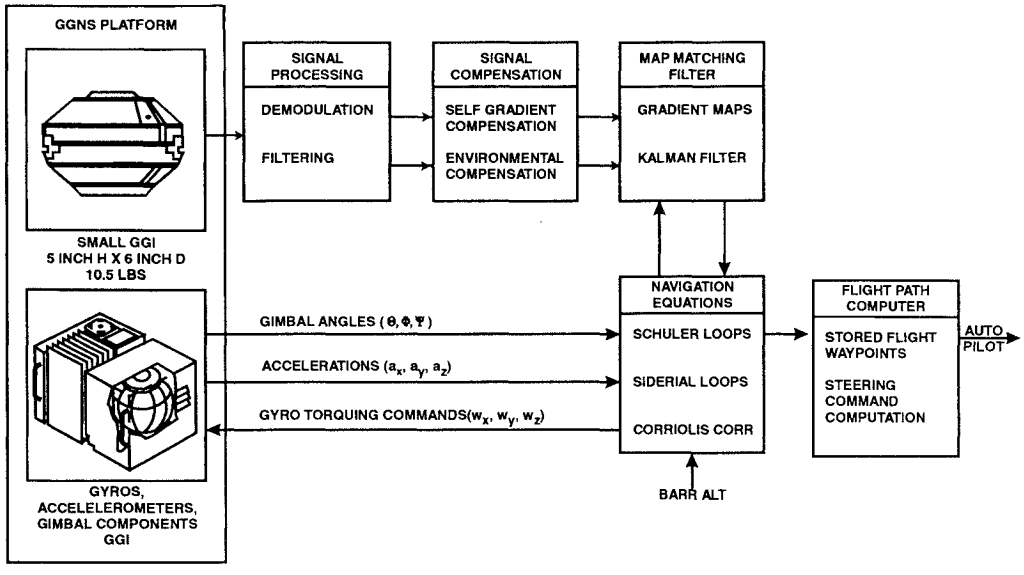

GRAVITY GRADIENT MAP MATCHING BLOCK DIAGRAM

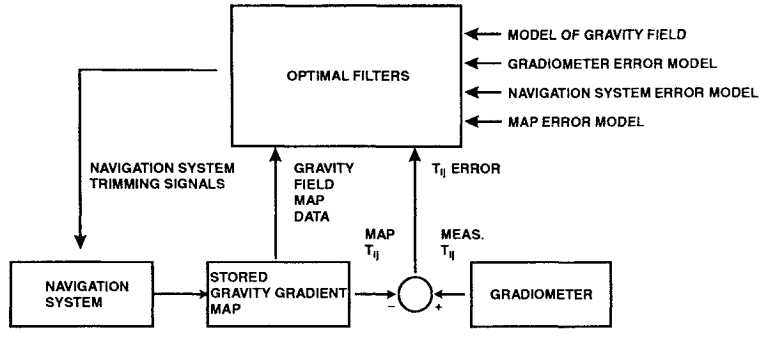

Fig. 1 Envisioned mechanization diagrams of the inertial/gradiometric navigation system (taken from Ref. 1).

sources. The residual errors, or the measured–stored gradient differences, are processed by the filter to passively update position in all three dimensions and to correct the INS. The filter uses traditional linear dynamic models of the INS and gradiometer error sources listed and applies corrections to all system components. Figure 2 shows the results of combined simulations and covariance error analyses performed by Affleck and Jircitano.[1] It plots bounded position errors [the horizontal in circular error probability (CEP) feet, the vertical in rms feet] as a function of gradiometer white noise levels and INS quality (characterized by gyro random drift). The simulations reached steady state within 15–20 km of travel under an assumed aircraft velocity of 360 km/h and a fixed aboveground altitude of 200 m. Figure 3 (also from Ref. 1) shows performance as a function of aboveground altitude and gradiometer noise, assuming a fixed, poor quality gyro drift of 0.01 deg/h. It will be shown in the next section that gravity gradient signal strengths rapidly attenuate with altitude, and this is reflected in Fig. 3. Unlike TERCOM, SITAN, and other terrain-based systems, a gradient matching system provides vertical position updates as well as horizontal.

Crucial requirements for the implementation of this autonomous system are geophysical databases and algorithms that can efficiently generate constant altitude grids of T_{ij} gravity gradient disturbances of sufficient accuracy and resolution. The generation of the stored gradient maps is only superficially addressed in Affleck and Jircitano.[1] The next three sections of this paper will focus on these issues and present efficient fast Fourier transform (FFT) algorithms that exploit 1) all available ground gravity, terrain elevation, and mass density databases and 2) the spectral sensitivities of the gravity gradiometer's signals.

II. Discriminating Between Terrain and Subterranean Gravitational Pulls

The gravitational potential at an at-altitude point (x, y, z), due to all surrounding masses of varying density ρ is given in m^2/s^2 potential units by the three-dimensional convolution

$$V(x, y, z) = G \iiint_{-\infty}^{\infty} \frac{\rho(\xi, \eta, \beta)}{\sqrt{(x-\xi)^2 + (y-\eta)^2 + (z-\beta)^2}} \, d\xi \, d\eta \, d\beta \tag{3}$$

The lack of knowledge of Earth mass density variability is by far the main theoretical obstacle to computing accurate, high-resolution, airborne grids of gravity gradients. Moreover, the onboard gravity gradiometer will sense not only the gravitational attraction of terrain above some adopted reference surface (e.g., mean sea level) but also that due to density variations beneath the reference surface. As will be shown in Sec. IV, density variations in the Earth's inner core and mantle are reflected mainly in the lower frequency end of the gravitational signal spectrum whereas terrain effects dominate the higher end. Since gravity gradient measurements mainly sense gravimetric features having spatial resolutions of 5 km or less (see Sec. IV), a gravity gradiometer is more sensitive to terrain effects than the longer wavelength geological effects. Still, the lack of knowledge of density variation (in the terrain and below) is the key theoretical stumbling block. As will be shown later in this section, if gridded terrain elevation data is supplemented with noninterpolated, ground gravity data of the same resolution, the unknown density variation can be bypassed. It is over areas lacking extensive ground gravity surveys that the density variation problem is paramount.

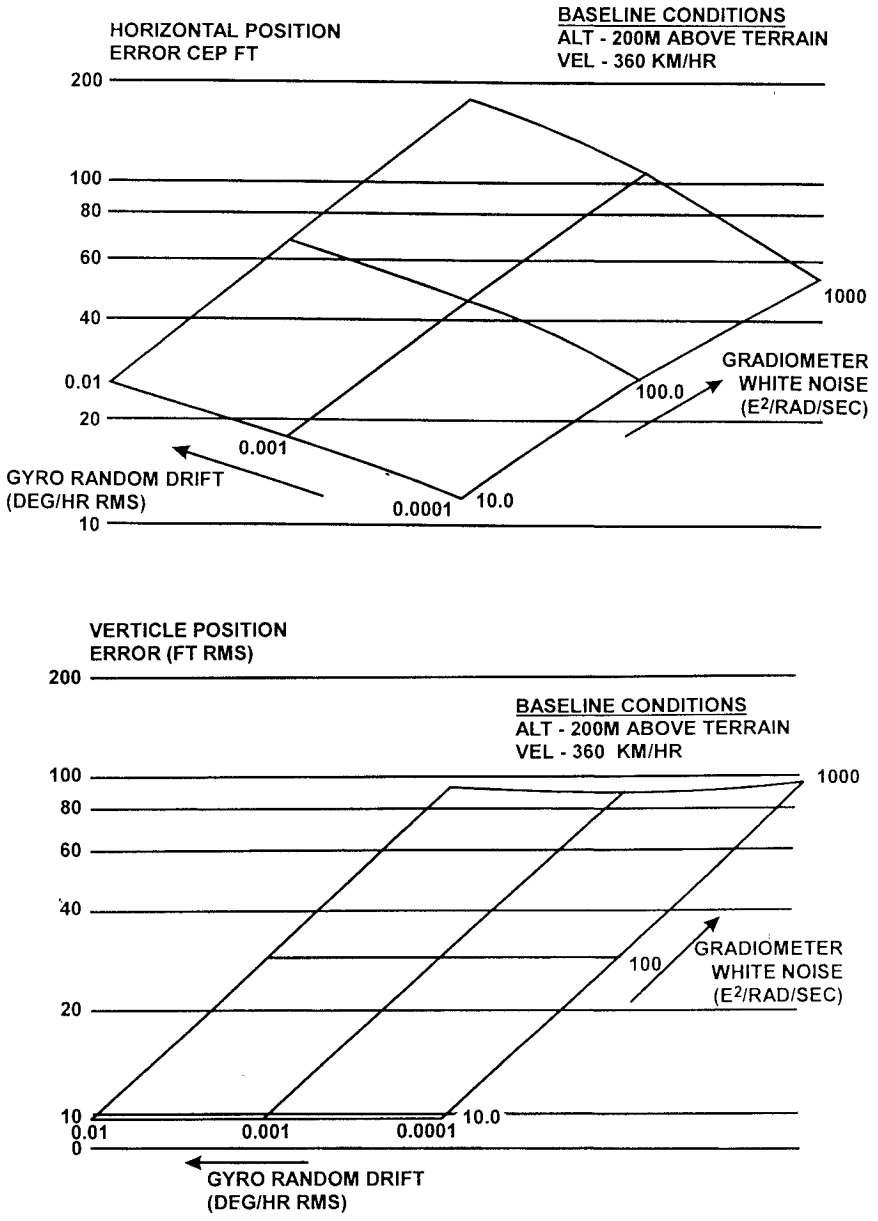

Fig. 2 Estimated position errors as a function of gradiometer noise, gyro drift, and the specified baseline conditions (taken from Ref. 1).

The convolution in Eq. (3) corresponds to multiplication in the frequency domain. Thus, the numerical implementation of the potential theory developed in this paper is based on highly efficient FFTs. Flat Earth approximations are adopted and the FFTs can be evaluated over grids as large as 700 km^2 (6 × 6 deg). The long wavelength signature of any available ground gravity data is first removed with a truncated set of global geopotential coefficients. The Earth surface resolution of the truncated harmonic degree n_t is approximately $(180/n_t) \cdot 100$ km, and this corresponds to the overall grid size of the input ground gravity/terrain elevation data. After the FFT algorithms are applied, the long wavelength components are restored at altitude. Owing to the four major pitfall areas of any discrete FFT pair application, namely, aliasing, spectral leakage, circular (nonlinear) convolution, and edge (Gibbs) effects, the at-altitude grids of gradient estimates must be confined to the central portion of the overall 6-deg square area. Popular remedies for the aforementioned concerns (e.g., cosine tapering windows, zero padding, etc.) are discussed in Gleason.[2]

Computer memory and storage limitations make execution of the three-dimensional FFT pairs related to Eq. (3) impractical. However, summing up a series of two-dimensional FFT pair-related layers (each layer related to a constant altitude) is tractable. For a constant altitude $z = h_d$, it can be proven for every $\beta\varepsilon(-\infty, \infty)$ that the two-dimensional Fourier transform (FT) of $G \cdot$ (reciprocal distance) contained in Eq. (3) is analytically given by

$$F\left\{\frac{G}{\sqrt{(x-\xi)^2+(y-\eta)^2+(h_d-\beta)^2}}\right\} = \frac{2\pi G}{\omega}\exp(-\omega|h_d-\beta|) \tag{4}$$

where the frequency parameter $\omega = \sqrt{(\omega_x^2+\omega_y^2)}$. For every constant $\beta_c\varepsilon(-\infty, \infty)$, let us denote the two-dimensional FT of the corresponding density surface as $R(\omega_x, \omega_y, \beta_c)$. Then for the constant estimation altitude $z = h_d$, the spectrum of Eq. (3) can be expressed as

$$\bar{V}(\omega_x, \omega_y, h_d) = \frac{2\pi G}{\omega}\int_{\beta=-\infty}^{\infty}\exp(-\omega|h_d-\beta|)\cdot R(\omega_x, \omega_y, \beta)\,d\beta \tag{5}$$

Citing Eq. (5), the two-dimensional spectrum of the disturbing potential T (due to all masses above the $\beta = 0$ reference height surface), evaluated along the $z = h_d$ surface, can be defined as

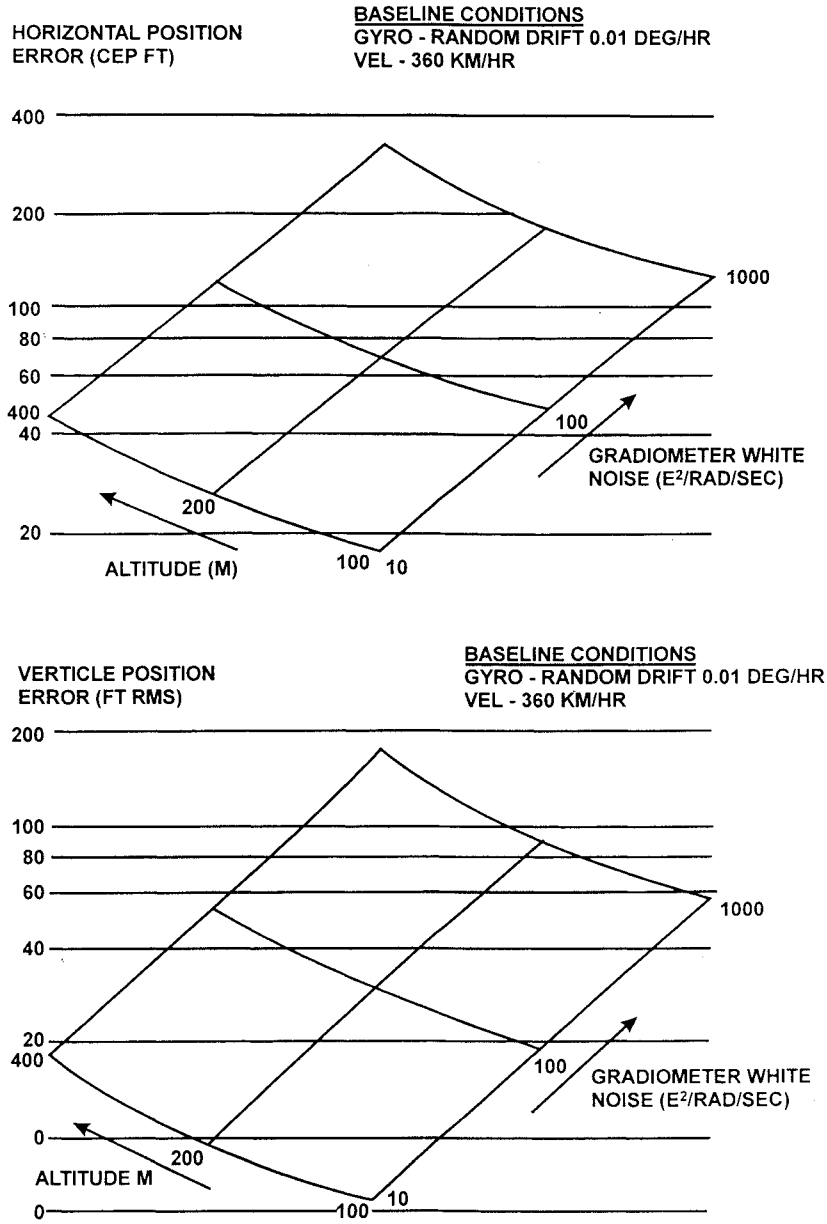

Fig. 3 Estimated position errors as a function of gradiometer noise, aboveground altitude, and the specified baseline conditions (taken from Ref. 1).

$$\bar{T}(\omega_x, \omega_y, h_d) = \frac{2\pi G e^{-\omega h_d}}{\omega}\left\{\int_{\beta=0}^{h_0} e^{\omega\beta}\cdot R(\omega_x, \omega_y, \beta)\,d\beta + \int_{\beta=h_0}^{h_d} e^{\omega\beta}\cdot R(\omega_x, \omega_y, \beta)\,d\beta\right\} + \frac{2\pi G e^{+\omega h_d}}{\omega}\int_{\beta=h_d}^{H} e^{-\omega\beta}\cdot R(\omega_x, \omega_y, \beta)\,d\beta \tag{6}$$

By subdividing the $(0, h_0)$, (h_0, h_d), and (h_d, H) elevation intervals into i, j, and k layers, respectively, Eq. (6) can be approximated as

$$\bar{T}(\omega_x, \omega_y, h_d) = \frac{2\pi G e^{-\omega(h_d - h_0)}}{\omega^2}\sum_i \exp[-\omega(h_0 - HT_i)] \times \{1 - \exp[-\omega(HT_i - HB_i)]\}\cdot R(\omega_x, \omega_y, i) + \frac{2\pi G}{\omega^2}\sum_j \exp[-\omega(h_d - HT_j)] \times \{1 - \exp[-\omega(HT_j - HB_j)]\}\cdot R(\omega_x, \omega_y, j) + \frac{2\pi G}{\omega^2}\sum_k \exp[-\omega(HB_k - h_d)] \times \{1 - \exp[-\omega(HT_k - HB_k)]\}\cdot R(\omega_x, \omega_y, k) \tag{7}$$

where the ith, jth, and kth layers are bordered by HB_i, HT_i, etc., and $R(\omega_x, \omega_y, i)$ denotes the two-dimensional FT of the ith density layer. Thus, one must assign a varying $\rho(m, n)^i$ density value for each $(m, n)^i$ space domain cell. As previously stated, density variation knowledge is quite limited. Adopting a crude constant upper-crustal density value of 2.67 g/cm^3 and denoting the mean terrain elevation of the (m, n) cell by $h^*(m, n)$, yields $\rho(m, n)^i = 2.67$, if $h^*(m, n) > HT_i$; $\rho(m, n)^i = 0$, if $h^*(m, n) < HB_i$; and $\rho(m, n)^i = 2.67[h^*(m, n) - HB_i]/[HT_i - HB_i]$, if $HB_i \le h^*(m, n) \le HT_i$.

Since $F\{T_{\text{north}}\} = F\{\partial T/\partial x\}$, $F\{T_{\text{east}}\} = F\{\partial T/\partial y\}$, and $F\{T_{\text{down}}\} = F\{-\partial T/\partial z\}$, let us denote the spectra obtained by placing a minus sign in front of the k-indexed summation in Eq. (7) by $\bar{\Theta}(\omega_x, \omega_y, h_d)$. If $h_0 < h_d < H$, then well-known analytical transfer functions yield the spectra of the first-order gravity disturbance vector components along the constant $z = h_d$ grid. They are given by

$$\begin{bmatrix} \bar{T}_N(\omega_x, \omega_y, h_d) \\ \bar{T}_E(\omega_x, \omega_y, h_d) \\ \bar{T}_D(\omega_x, \omega_y, h_d) \end{bmatrix} = \begin{bmatrix} \bar{T}(\omega_x, \omega_y, h_d)\cdot i\omega_x \\ \bar{T}(\omega_x, \omega_y, h_d)\cdot i\omega_y \\ \bar{\Theta}(\omega_x, \omega_y, h_d)\cdot \omega \end{bmatrix} \tag{8}$$

The three space domain T_i gravity disturbance vector components (commonly measured in mGal or 10^{-5}m/s^2 acceleration units),

along the constant $z = h_d$ grid, are obtained by taking the two-dimensional inverse FTs of $\bar{T}_N$, $\bar{T}_E$, and $\bar{T}_D$. For the case where $h_d > H$, there is no k-indexed summation in Eq. (7) whatsoever and, thus, the $\bar{\Theta}$ entry in Eq. (8) is replaced by $\bar{T}$.

Again applying applicable transfer functions yields the spectra of the six unique values of the symmetric, zero-trace, second-order T_{ij} gravity gradient disturbance tensor. They are

$$\begin{bmatrix} \bar{T}_{NN}(\omega_x, \omega_y, h_d) \\ \bar{T}_{NE}(\omega_x, \omega_y, h_d) \\ \bar{T}_{ND}(\omega_x, \omega_y, h_d) \\ \bar{T}_{EE}(\omega_x, \omega_y, h_d) \\ \bar{T}_{ED}(\omega_x, \omega_y, h_d) \\ \bar{T}_{DD}(\omega_x, \omega_y, h_d) \end{bmatrix} = \begin{bmatrix} \bar{T}(\omega_x, \omega_y, h_d) \cdot \left(-\omega_x^2\right) \\ \bar{T}(\omega_x, \omega_y, h_d) \cdot (-\omega_x \omega_y) \\ \bar{\Theta}(\omega_x, \omega_y, h_d) \cdot (i\omega_x \omega) \\ \bar{T}(\omega_x, \omega_y, h_d) \cdot \left(-\omega_y^2\right) \\ \bar{\Theta}(\omega_x, \omega_y, h_d) \cdot (i\omega_y \omega) \\ \bar{T}(\omega_x, \omega_y, h_d) \cdot (\omega^2) \end{bmatrix} \tag{9}$$

and the two-dimensional inverse FTs yield the desired $z = h_d$ at-altitude, space domain T_{ij} gravity gradient disturbances (again measured in 10^{-9}/s^2 Eotvos units). Obviously, the finer the resolution of the input terrain elevation data and the ith, jth, and kth layers, the closer the discrete computations will approximate Eq. (6). The nominal 2.67 g/cm^3 density model is clearly the shortcoming of the preceding algorithm. The remainder of this section will overview a density-free algorithm that can rigorously upward/downward ground gravity and terrain elevation gridded data to specified constant altitudes and optimally transform the information content to airborne T_{ij} gravity gradient disturbance grids. Unfortunately, there are large regions of the Earth where high-resolution ground gravity surveys have never been conducted. For such areas, one must resort to the nonoptimal approach already outlined.

Absolute and relative gravimeter measurements are taken on the Earth's actual and irregular surface. Such ground gravity measurements must be reduced to a level surface, such as the approximately mean sea level geoid, before they can be upward/downward continued and transformed (using the laws of potential theory) to airborne grids of T_i and T_{ij} gravity and gravity gradient disturbances. Traditional Bouguer reductions and terrain corrections remove the effects of the terrain between the Earth's surface and the geoid by using 1) the nominal density value of 2.67 g/cm^3 and 2) a subsequent free-air reduction down to the geoid, which approximates the vertical gradient of actual gravity, $\partial \boldsymbol{g}/\partial z$ = normal gravity gradient + anomalous gravity gradient = $\partial\gamma/\partial z + \partial(\Delta \boldsymbol{g})/\partial z$, by its $\partial\gamma/\partial z$ normal counterpart (implied by the homogeneously dense reference ellipsoid and =0.3086 mGal/m =3086 Eotvos units). Based on the theory of Moritz,[3] Gleason[2] presents a self-inclusive description of an optimal, FFT-based analytical continuation (rather than reduction) of gridded, ground-referenced T_D and terrain elevation measurements to any specified level surface. Once again, the long wavelength effects of the ground gravity data are removed with a set of geopotential coefficients truncated at the harmonic degree n_t corresponding to the ground resolution of the overall gravity/terrain elevation grid size. After the ground-referenced T_D and terrain data have been continued to the specified level surface, the information content can be transformed to constant-altitude, airborne grids of T_i and T_{ij} gravity and gravity gradient disturbances using modified versions of the transfer functions listed in Eqs. (8) and (9). As before, long wavelength effects are restored at altitude after all of the FFT and upward/downward continuations steps have been implemented. The continuation is completely free of terrain density assumptions, actually solves for the $\partial(\Delta \boldsymbol{g})/\partial z$ vertical gradient of anomalous gravity, and rigorously obeys all of the laws of potential theory. As such, the final optimally estimated grids of airborne T_{ij} gradients should agree with actual T_{ij} values at all points external to the Earth's irregular surface.

The intermediate, level surface-referenced, gravimetric information can also be brought back up (or down) to the Earth's irregular surface through the use of two-dimensional FFT pair implemented Taylor series and transformed to any Earth surface T_i or T_{ij} quantity. As shown in Gleason,[2] subarc-s agreement was obtained between analytically continued deflections of the vertical (i.e., T_N and T_E), referenced to the Earth's actual surface, and 400 very accurate astrogeodetic deflection measurements taken at White Sands. The White Sands study involved a 6-deg square of gravity and terrain data having a grid resolution of 1-arc min (2 km). It is strongly noted that this optimal, density-free approach requires gridded sets of both ground gravity and terrain elevation data.

III. Comparing Optimal Airborne T_i and T_{ij} Estimates and Nonoptimal Estimates

Gridded, 1-arc min (2-km resolution) mean T_D and terrain elevation values over a 6-deg square area surrounding White Sands were supplied by the Defense Mapping Agency Aerospace Center, St. Louis. The accuracies of the T_D values ranged from 1 to 12 mGals with the overall rms of the errors being 2.6 mGals. The accuracy of the mean terrain elevations was a uniform 3 m. The minimum and maximum elevations over the 6-deg square area were 622 and 3655 m, corresponding to the Sec. II variables h_0 and H, respectively. The h_d constant altitude of the airborne estimates was set to 3700 m. The effects of the first 36 harmonic degrees were accounted for with the OSU86F global gravity model. The number of Sec. II, i layers (between sea level and h_0) was simply set to 1, the number of j layers (between h_0 and h_d) was set to 10, and the number of k layers between H and h_d is 0 in this scenario. Increasing the number of j layers, of course, improves the discrete two-dimensional FFT approximations.

Figure 4 plots the 2-km resolution terrain of the central 1-deg square over which our at-altitude predictions are limited. The minimum and maximum elevations within this 1-deg square were 1182 and 2683 m, respectively. Figure 5 plots the 1-arc min mean, ground-referenced T_D gravity disturbances over the central 1-deg square. One can note the expected visual correlation between Figs. 4 and 5. Figure 6 plots the errors in the central 1-deg T_D. Many of the T_D are interpolated values (especially over extremely rugged terrain cells). Comparing Figs. 4 and 6 reveals it is the interpolated values possessing the higher error estimates. Gleason[2] showed this extensive use of interpolated ground gravity data resulted in a significant loss of high frequency information in predicted, ground-referenced T_N and T_E deflections of the vertical (using the optimal estimation technique) located in areas lacking actual gravity measurements.

Figure 7 plots T_E (h_d = 3700 m) at-altitude estimates over the central 1-deg area. The top surface plot of the figure refers to nonoptimal estimates based on terrain elevation data only using the nominal $\rho = 2.67$ density model. The bottom surface plot refers to the

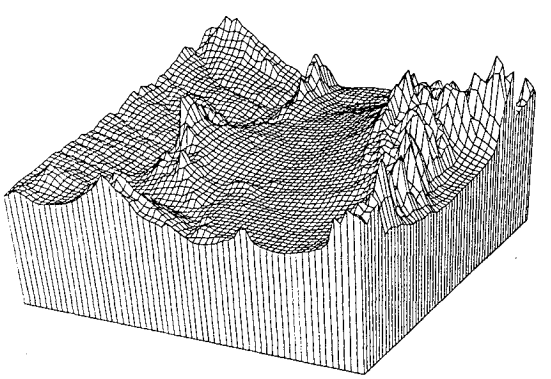

Fig. 4 Central 1-deg square of overall 6 × 6 deg White Sands terrain database used; resolution is 1 arc min or roughly 2 km.

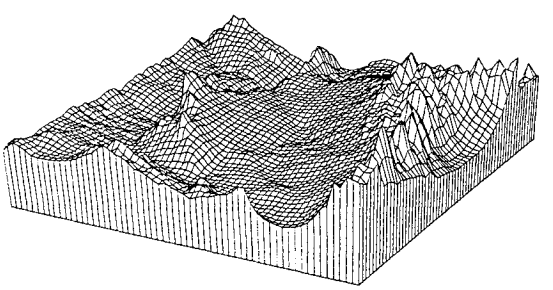

Fig. 5 Mean 1-arc min ground gravity values of White Sands central 1-deg square.

Table 1 Statistics on two sets of at-altitude T_i gravity disturbance estimates, all units in mGals, resolution is 1 arc min

Qty.	Range: Terrain only	Range: Terrain and gravity	Bias (average diff.)	Postbias rms of terr. and gravity-terr. only diffs.
T_N	(−73,6)	(−48,17)	17	6
T_E	(−2,62)	(−20,22)	29	8
T_D	(−3,77)	(−32,45)	25	11

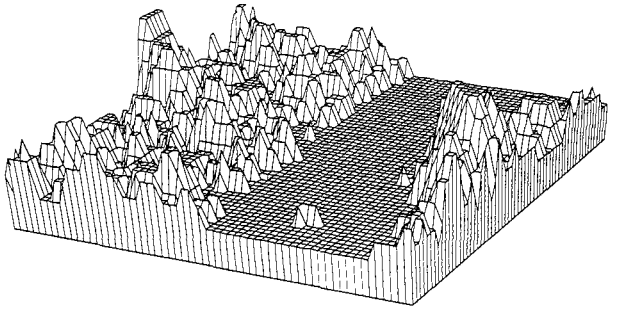

Fig. 6 Errors in White Sands central 1-deg ground gravity values; range: 1–12 mGals.

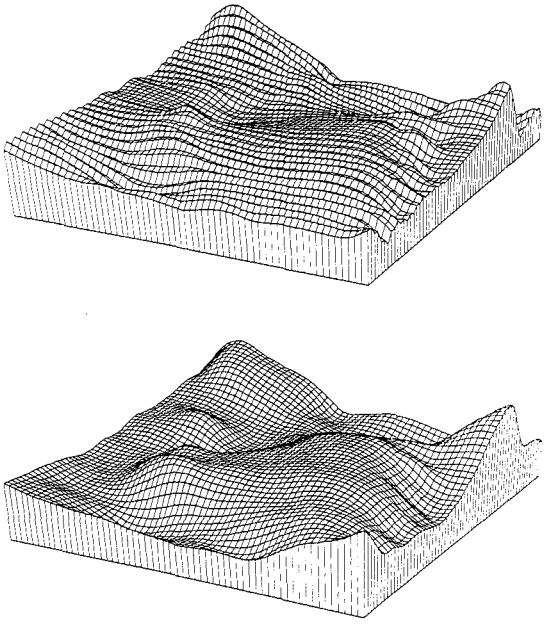

Fig. 7 Central 1-deg T_E (altitude = 3700 m) estimates: top surface plot: from terrain data only and ρ = 2.67 g/cm^3; bottom surface plot: from terrain data and ground gravity data; bias between two estimate sets: 29 mGals; postbias rms$_{\text{overall differences}}$: 8 mGals.

optimal density-free estimates based on both ground gravity and terrain elevation data. One can see that the two algorithms estimate similar at-altitude T_E trends (crucially important for real-time matching with the single flight-path profile of gradient measurements). Table 1 is a statistical summary of the optimal vs nonoptimal gridded estimates for all three T_i. The significant bias between the two estimate sets is clearly due to the crude nominal density model assumed in the nonoptimal algorithm. As alluded to earlier, the smaller absolute numerical range of the smoother, ground-gravity-based, airborne estimates is due to the many interpolated gravity values assigned over the rugged (higher elevation) 1-arc min cells.

Figures 8 and 9 plot T_{NN} and T_{ND} ($h_d = 3700$ m) at-altitude gravity gradient disturbance estimates over the central 1-deg area. Again, the top surface plot of each figure refers to predictions based solely on terrain elevation data and the bottom plot depicts optimal estimates based on ground gravity and terrain data. Table 2 is a statistical summary for the 6 unique sets of airborne T_{ij} second-order gravity gradient disturbance estimates.

Table 2 Statistics on two sets of at-altitude T_{ij} gravity gradient disturbance estimates, all units in Eotvos, resolution is 1 arc min

Qty.	Range: Terrain only	Range: Terrain and gravity	Bias (average diff.)	Postbias rms of terr. and gravity-terr. only diffs.
T_{NN}	(−120,47)	(−64,39)	1.6	7.5
T_{EE}	(−100,37)	(−34,24)	0.2	5.7
T_{DD}	(−41,168)	(−42,72)	1.4	10.7
T_{NE}	(−29,49)	(−17,26)	1.7	3.6
T_{ND}	(−100,84)	(−67,56)	1.9	8.4
T_{ED}	(−83,108)	(−26,38)	1.7	18.9

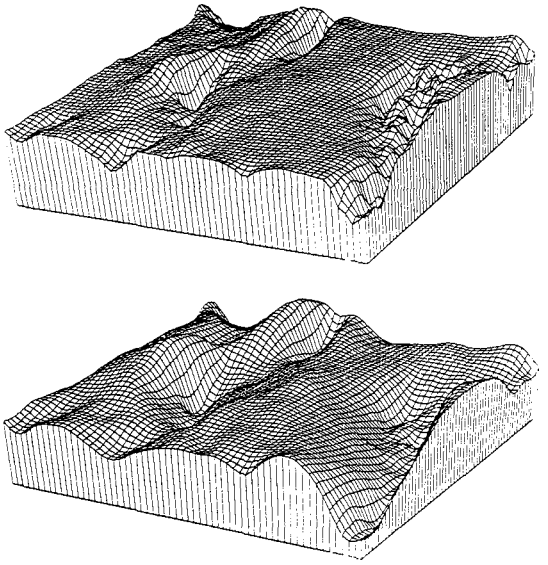

Fig. 8 Central 1-deg T_{NN} (altitude = 3700 m) estimates: top surface plot: from terrain data only and ρ = 2.67 g/cm^3; bottom surface plot: from terrain data and ground gravity data; overall rms$_{\text{differences}}$: 7.5 Eotvos.

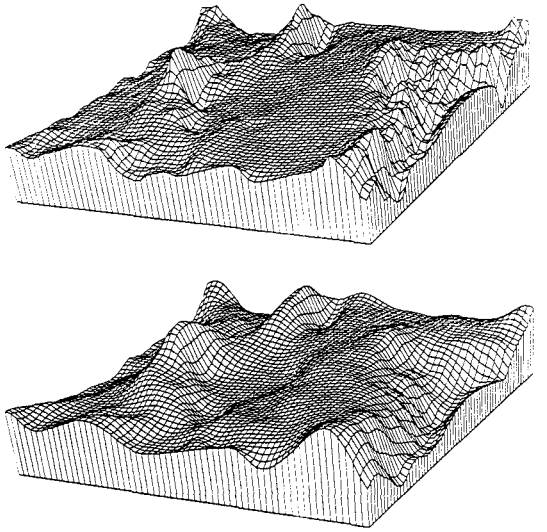

Fig. 9 Central 1-deg T_{ND} (altitude = 3700 m) estimates: top surface plot: from terrain data only and ρ = 2.67 g/cm^3; bottom surface plot: from terrain data and ground gravity data; overall rms$_{\text{differences}}$: 8.4 Eotvos.

As expected, the significant constant biases separating the sets of first-order T_i estimates vanish when one performs subsequent differentiations to obtain the second-order T_{ij}. Once again the smoother, interpolated ground gravity database limited the absolute numerical range of the related at-altitude gradient estimates. Figures 8 and 9 again illustrate that the two estimation techniques predict similar airborne gradient trends. The fact that the bias-free T_{NN}, T_{EE}, and T_{DD} in-line gradient estimate differences have overall rms in the

(5, 10) Eotvos interval bodes well for at-altitude gradient predictions over inaccessible areas lacking extensive ground gravity data. Of equal importance, the test results of this section reveal that reliance on interpolated ground gravity data can be detrimental to the cause since it results in a heavy loss of high-frequency information in the local field. As will be shown in the next section, along these higher frequencies the power spectrum density (PSD) of terrain-implied local gravity fields exceeds that of local geology or subterranean-implied fields. It will also be shown that low-flying gravity gradiometers are more sensitive to the short wavelength features dominated by the terrain.

IV. Frequency Range Sensitivities of T_i Gravity and T_{ij} Gravity Gradient Disturbances

The gravity disturbance, at some exterior point P, is defined as actual gravity at P minus the so-called normal gravity at P. Normal gravity, implied by a homogeneously dense reference ellipsoid that approximates the Earth in shape and size, is easy to compute (see Heiskanen and Moritz[4]). Assuming a spherical Earth model, the geocentric radial component of the local plumb line or $\boldsymbol{g}$ vector is given by $g_r = -GM/r^2 + \delta g_r$ where the harmonic degree n, order m, frequency component representation of the δg_r radial component of the $\delta \boldsymbol{g}$ gravity disturbance vector at $(r, \phi, \lambda)_P$, is given by the infinite $\bar{P}_{nm}$ Legendre series

$$\delta g_r = \frac{-GM}{r^2} \sum_{n=2}^{\infty} (n+1) \left(\frac{R_{\text{Earth}}}{r} \right)^n \times \sum_{m=0}^{n} (\bar{C}_{nm} \cos m\lambda + \bar{S}_{nm} \sin m\lambda) \bar{P}_{nm}(\sin \phi) \tag{10}$$

where the spatial resolution of the nth harmonic degree or frequency component is again approximately $(180/n) \cdot 100$ km, and the unitless $(\bar{C}_{nm}, \bar{S}_{nm})$ coefficient set makes up the spectrum of the anomalous or disturbing gravity field. Similarly, the second-order radial gravity gradient is given by $g_{rr} = 2GM/r^3 + \delta g_{rr}$ where the gradient disturbance is given by

$$\delta g_{rr} = \frac{GM}{r^3} \sum_{n=2}^{\infty} (n+1)(n+2) \left(\frac{R_{\text{Earth}}}{r} \right)^n \times \sum_{m=0}^{n} (\bar{C}_{nm} \cos m\lambda + \bar{S}_{nm} \sin m\lambda) \bar{P}_{nm}(\sin \phi) \tag{11}$$

The PSDs of δg_r and δg_{rr} are the collective sets of all of their respective harmonic degree n (frequency) variances. For each quantity, the individual degree n variance is given by

$$\delta g_{r_n}^2 = \left(\frac{GM}{r^2} \right)^2 (n+1)^2 \left(\frac{R_{\text{Earth}}}{r} \right)^{2n} \sum_{m=0}^{n} (\bar{C}_{nm}^2 + \bar{S}_{nm}^2) \tag{12}$$

and

$$\delta g_{rr_n}^2 = \left(\frac{GM}{r^3} \right)^2 (n+1)^2 (n+2)^2 \left(\frac{R_{\text{Earth}}}{r} \right)^{2n} \sum_{m=0}^{n} (\bar{C}_{nm}^2 + \bar{S}_{nm}^2) \tag{13}$$

A quick analysis of Eqs. (10–13) reveals that although the δg_{rr} gradient disturbance signal attenuates much faster with altitude, by $1/r^3$ vs $1/r^2$ for δg_r, it reflects much more, finer resolution, higher harmonic degree n, frequency component information. These higher frequency components represent the localized anomalous gravity field near the computation point in which terrain effects dominate (this will be shown later). Current sets of $(\bar{C}_{nm}, \bar{S}_{nm})$ geopotential coefficients extend through $n = m = 360$, supplying global gravity signal information down to resolutions of 50 km. The $n > 360$ power spectra components are, in practice, approximated using well-known global gravity spectrum models. Examples include Kaula's[5] famous rule of thumb, which empirically approximates each $\sum(\bar{C}_{nm}^2 + \bar{S}_{nm}^2)$ degree n variance as $10^{-10}(2n+1)/n^4$ (there are $2n+1$ nonzero coefficients per degree n) and the analytical degree n variance models such as Moritz[3] and Tscherning and Rapp.[6]

Table 3 δg_r gravity disturbance and δg_{rr} gravity gradient disturbance spectral sensitivities

Qty.	Spatial resolution; harmonic degree n frequency component range,%			
	>500 km, $n \leq 36$	(50 km, 500 km), $37 \leq n \leq 360$	(5 km, 50 km), $361 \leq n \leq 3600$	<5 km, $n \geq 3601$
δg_r	22	42	33	3
δg_{rr}	0	1	39	60

Table 3 shows, by percentage of the entire $(n \Rightarrow \infty)$ signal, the harmonic frequency or spectral sensitivity of δg_r and δg_{rr}, using the Tscherning and Rapp[6] power spectra model. One can note the δg_r gravity disturbances ($\cong \delta g_{\text{plumb line}}$ disturbances measured by levelled gravimeters) mainly reflect mass/density variations having spatial resolutions of 50 km or larger. By contrast, second-order δg_{rr} gradient disturbances, measured by a gravity gradiometer, mainly sense mass/density variations possessing spatial resolutions of 5 km or less. Thus, a gravity gradiometer is the instrument of choice to detect the gravitational attractions caused by extremely high resolution, oncoming terrain.

It is strongly reiterated that the strength of the sensed δg_{rr} signal, $\cong G(\delta M)/d^3$ where δM is the dominant mass anomaly sensed (e.g., local terrain feature), attenuates quickly with altitude d. The next section will examine how this fact puts stringent sensitivity and feature resolution requirements on a gradiometer when used in an oncoming terrain avoidance application.

For such an application, it is crucial to know the power in the local terrain-implied and subterranean, geology-implied gravity fields at various wavelengths. If ground gravity data are lacking, one would like to focus in-flight on the wavelengths and frequencies dominated by the terrain and suppress/dampen those dominated by the geology. Assuming a terrain density of 2.67 g/cm^3, the well-known Bouguer, terrain-implied gravity factor is 0.112 mGal/m of terrain above the adopted reference surface (e.g., mean sea level or the geoid). This Bouguer factor was used to convert White Sands 30-arc s (1-km resolution) mean terrain elevations into terrain-implied gravity anomalies or disturbances. After a mean and trend were removed from these terrain-implied g values, an isotropic, two-dimensional, first-order Markov PSD model was fitted to the residual terrain-implied gravity field. A baseline third-order Markov PSD model was then fitted to the White Sands 1-arc min (2-km resolution) mean ground gravity anomaly database, after terrain effects were removed from the actual gravity values.

Figure 10 compares the terrain-implied and geology-implied PSD models. One can note that for wavelengths >35 km, the terrain PSD is weaker than the geology PSD, but over shorter wavelengths the terrain PSD dominates. Clearly the crossover wavelength will be shorter over less turbulent (i.e., flatter) terrain. Using this approach, apriori crossover wavelengths can be estimated over any area where dense gravity and topography surveys have been conducted. High-pass (≥crossover frequency) filtered, terrain-implied, at-altitude gradient grids could then be real-time matched with corresponding high-passed measurements taken by the gradiometer. If the grids of gradients were nonoptimally estimated from terrain data only (i.e., if no ground gravity data were available), the unwanted effects of the longer wavelength geology structures, weakly sensed by the gradiometer anyway, could be dampened even further (although the exact crossover wavelength would be unknown).

As shown in Table 3, most of the total gravity gradient disturbance signal is due to localized mass concentrations having spatial resolutions of 50 km or less. Moreover, this signal mainly senses mass anomalies having resolutions of 5 km or less. Thus, a significant portion of the total δg_{rr} signal survives even a very high high-pass filter (similar situations exist for the other on- and off-diagonal elements of the gradient disturbance tensor). Simply put, the high-frequency sensitivities of a gravity gradiometer allow it to react to nearby terrain and make it relatively insensitive to long wavelength geologic structures. Obviously the aboveground altitude, aircraft velocity, and the gradiometer's sampling rate and noise level are the key parameters that determine possible gradient resolution and accuracy,

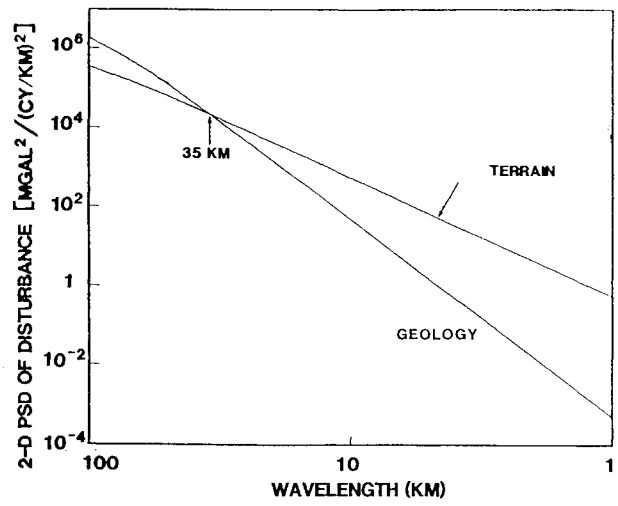

Fig. 10 PSD of terrain-implied and subterranean-implied T_D gravity disturbance field over White Sands.

measured along the flight profile. The next section will show how these critical parameters control the feasibility of real-time terrain avoidance and will examine the performance levels of current and near-future gradiometer systems.

V. Inertial Navigation System and Gradiometer Performance Challenges Related to Oncoming Terrain Avoidance

The numerical and analytical studies of the previous sections involved gridded terrain elevation resolutions of 1 and 2 km. In a low-flying, high-velocity, oncoming terrain detection/avoidance scenario, one is obviously concerned about terrain features having substantially finer resolutions. The adopted aboveground altitude will determine the required terrain resolution to be sensed. Factors that will determine the actual resolution sensed by the airborne gradiometer are 1) the aircraft's velocity, 2) the aboveground altitude (recall gradients attenuate by $1/d^3$), 3) the gradiometer's noise level (in the sense of its average, double-sided PSD of gradient noise, measured in Eotvos^2/hertz units, or single-sided band noise PSD, in Eotvos/$\sqrt{}$hertz), 4) the instrument's gravity gradient production rate (not the same as its raw sampling rate; see subsequent discussion), and 5) the cutoff frequency of any low-pass filter used to demodulate the gravity gradient signals and remove any uncompensated, high-frequency error sources still plaguing the measurements.

To get a better understanding of the interrelationships among these five parameters, a quick overview of the design of the gravity gradiometer survey system (GGSS), the only gradiometer that currently can be operated on a moving platform, will be presented. The GGSS was funded by the Defense Mapping Agency, is owned by the Air Force's Phillips Laboratory, and was fabricated in the mid 1980s by Bell Aerospace Textron. For a more detailed description of the GGSS, see Jekeli.[7]

The fundamental units of the GGSS are its three mutually orthogonal, gravity gradiometer instruments (GGIs). Each GGI possesses a set of four pendulous force rebalance type accelerometers. The four accelerometers are placed pairwise on a circular rotating plate such that the sensitivity axes point along sides of an inscribed square. These axes of oppositely positioned accelerometers point in opposite directions so that when their signals are summed, the common mode linear plate acceleration cancels. Differencing the two summed quantities cancels out the rotational accelerations of the plate. What is left is a measure of the gradient of gravity across the 15-cm accelerometer baseline (along with other nonlinear accelerations which need to be compensated for). In the instrument or sensor frame, each GGI provides two outputs related to the gravity gradients associated with the two axes in the plane of rotation: the cross gradient and one-half the difference of the two in-line gradients. Exploiting the symmetry of the gradient tensor and Laplace's equation (zero trace property), all nine gradients of gravity are attainable from the trio of GGIs. The GGIs are mounted on a local-stabilized, inertial platform (see Fig. 1). The platform is inertially stabilized by 3 gimbals controlled by two 2-deg-of-freedom gyroscopes and a dedicated (non-GGI) set of three orthogonal accelerometers, which also supplies short term navigation (which would be passively updated by the real-time gradient matching described in Sec. I).

The total array of 12 GGI accelerometers is dependent on both mechanical and electronic feedback/adjustment loops to control and compensate many (but not all) of the error sources that would otherwise cloak the relatively small gravity gradient signals. The most important of the control/compensation mechanisms is the shifting of the desired gravity gradient signal to a frequency regime far away from where most of the error power resides. This is done by rotating the plate at 0.25 Hz or 1 revolution every 4 s and exploiting the fact that the gravity gradients modulate at twice the rotation frequency since, if the pairwise accelerometers are identical (which they are not), the plate assumes the same orientation with respect to the gravity field every half-rotation. Errors due to accelerometer scale factor imbalances and the nonorthogonality of the accelerometer pairs are modulated at once the rotation rate and can be sensed and corrected by electronically adjusting the proof mass of each accelerometer. Errors due to accelerometer misalignments and sensitivities to nonlinear accelerations (other than the gravity gradient) are similarly sensed and corrected for continuously by dithering and shaking each GGI at specified frequencies.

The raw modualted GGI signals are currently passed at a sampling rate of 16 Hz to a computer where they are further compensated for centripetal and self-gradient effects. The latter are unwanted gravitational effects of the platform, all nearby structures, and the vehicle itself. They are mathematically functions of the (roll, pitch, yaw) angles describing the inner azimuth gimbal with respect to the vehicle. The GGI gravity gradient signals are then demodulated with a low-pass filter (which also cuts off uncompensated thermal-Browninan error sources) and the final gradients are actually produced at intervals of 1 s. The filter's cutoff frequency was set at 0.06 Hz (17-s time interval) for the 1987 flight test of the GGSS involving an aircraft speed of 400 km/h. This limited sensed feature resolutions to wavelengths of 1.9 km. The average level of gradient noise during the test flight was about 900 Eotvos^2/Hz which corresponds to, for a 10-s integration time, an rms error of around 10 Eotvos.

To get an initial feel for required gradiometer and INS performance specifications, the reader is again referred to Figs. 2 and 3 (both taken from Ref. 1). From Fig. 2 one sees if 1) the proposed passively updated INS/gradiometric navigation system possessed the aforementioned gradiometer white noise level of 900 Eotvos^2/Hz, 2) the aircraft is traveling at 360 km/h, 3) the aboveground altitude remains fixed at 200 m, and 4) the INS's gyro random drift rates range from 0.0001 deg/h to 0.01 deg/h; then the estimated range of bounded horizontal position error is about 60–200 ft (CEP) and the estimated vertical position error is around 90 ft (rms). Figure 3 refers to a fixed, poor INS gyro drift rate of 0.01 deg/h and adopts an aboveground altitude range of 100–400 m. Again for a gradiometer white noise level of 900 Eotvos^2/Hz, Fig. 3 shows an estimated 100–300+ ft (CEP) horizontal position error range and an estimated 60–150+ ft (rms) vertical position error. Figure 3 clearly illustrates the adverse effects of attenuating the gravity gradient signal with increased altitude.

Bell Aerospace Textron is currently fabricating an enhanced, single GGI (with respect to the vertical spin axis), stationary gradiometer for the Defense Nuclear Agency (DNA). Its rotating GGI plate will possess eight accelerometers (rather than the GGSS four) and revolve at a dramatically increased velocity. The pairwise accelerometer baselines will be doubled to 30 cm, which will make a much stronger gravity gradient signal-to-noise ratio. Adjusting these three design parameters can theoretically lead to a near-continuous raw sampling of the modulated GGI signals. However, the three parameters that dictate the feasibility of gravity gradiometry for terrain avoidance are 1) the cutoff frequency of the final filter suppressing all uncompensated, thermal-Brownian error sources, 2) the actual gradient production rate, and 3) the final gradient noise level. Bell's projected noise level for the DNA gradiometer is 1 Eotvos^2/Hz at a gradient production rate of 1 s. Further improvements, of course, could be pursued in a next-generation Bell device.

Scientists at the Johns Hopkins Applied Physics Laboratory are developing a room-temperature, stationary gravity gradiometer with a projected static noise level of 0.1 Eotvos and a sampling rate up to 100 Hz. The University of Maryland is developing a high-accuracy, superconducting (cryogenic) gradiometer with projected accuracies of 10^{-4} Eotvos in a stationary mode and 10^{-2} Eotvos on a moving base. The engineering challenges at hand include substantial improvements in 1) continuous compensations of accelerometer misalignments and scale factor mismatches due to material aging and temperature/pressure changes, 2) near-absolute platform stabilization in an inertial reference frame, 3) self-gradient compensation techniques, and 4) identification and compensation of more of the thermal-Brownian noise sources currently unaddressed and, therefore, cut off in a resolution robbing final demodulation type filter.

For a terrain avoidance application involving moving-base measurements, enhancing terrain feature resolvability is just as important as decreasing the gradient noise levels. As alluded to earlier, the applicable relationship is

vehicle velocity = (attainable wavelength)

× (cutoff frequency of final demodulation type filter)

Thus, for an aircraft speed of 1 Mach it is seen that 10-, 50-, and 100-m gravity field wavelength detections (5-, 25-, and 50-m resolutions) require cutoff frequencies of about 33, 7, and 3 Hz, respectively. Therefore, a dramatic adjustment needs to be made to the 1987 GGSS airborne cutoff frequency of 0.06 Hz to address the demanding requirements of oncoming terrain detection/avoidance. At the same time, the increased cutoff frequency can not result in increased gradient noise levels. It is left to the gradiometer fabrication community to engineer the needed noise and resolution specifications into an optimal gravity gradiometer of the 21st century. For additional recent developments and applications of gravity gradiometery, one is referred to Driscoll et al.[8]

VI. Concluding Remarks

This paper has shown that gravity gradiometry faces theoretical and engineering/design challenges that must be met before the technology can be integrated with an INS to passively navigate and avoid oncoming terrain. The chief theoretical obstacle, discriminating between local terrain-implied and local subterranean-implied (geology) gravity fields, can become moot if future global, gridded, ground gravity files take on the same high resolutions of current and future terrain elevation files. This paper has also shown the lack of such dense ground gravity data can be circumvented by limiting the real-time passive updating mechanization, namely, gravity gradient matching between the measured flight-path profile of gravity gradients and precomputed, stored, constant-altitude grids of terrain-implied gradients, to the higher frequency components of the local gravity field's spectrum. It is over the high end of the spectrum that the terrain effects dominate the subterranean effects and that the gradiometer's signal is most sensitive.

The main engineering challenge is to build a gradiometer system capable of producing low-noise gravity gradients (different than a noisy raw sampling) at a rate high enough to sense fine-resolution terrain effects from a high-speed aircraft. Concurrently, a substantial reduction in the presently uncompensated thermal-Brownian noise sources will be required. Meeting these design requirements will clearly enhance the performance of gravity gradiometry in the less demanding applications of underground structure detection and characterization, mineral and oil explorations, and airborne and spaceborne gravity surveys. The gravity gradiometer is a magnificent instrument that addresses a diverse array of highly laudable objectives. It is hoped the advent of the 21st century will bring it to its deserved place along the forefront of the high-technology stage.

References

[1]Affleck, C. A., and Jircitano, A., "Passive Gravity Gradiometer Navigation System," *Proceedings of the IEEE's Position Location and Navigation Symposium (PLANS)*, 1990, pp. 60–66.

[2]Gleason, D. M., "Obtaining Earth Surface and Spatial Deflections of the Vertical from Free-Air Gravity Anomaly and Elevation Data Without Density Assumptions," *Journal of Geophysical Research*, Vol. 95, No. B5, 1990, pp. 6779–6786.

[3]Moritz, H., *Advanced Physical Geodesy*, Abacus Press, Tunbridge Wells, Kent, England, UK, 1980.

[4]Heiskanen, W. A., and Moritz, H., *Physical Geodesy*, W. H. Freeman, San Francisco, 1967.

[5]Kaula, W. M., *Theory of Satellite Geodesy*, Blaisdell, Waltham, MA, 1966.

[6]Tscherning, C., and Rapp, R., "Closed Covariance Expressions for Gravity Anomalies, Geoid Undulations, and Deflections of the Vertical Implied by Anomaly Degree Variance Models," Dept. of Geodetic Science, Rept. 208, Ohio State Univ., Columbus, OH, 1974.

[7]Jekeli, C., "The Gravity Gradiometer Survey System (GGSS)," *EOS*, Vol. 69, No. 8, 1988, pp. 105, 116, 117.

[8]Driscoll, M. L., Heller, W. G., and White, J. V., "Multisensor Detection of Tunnels and other Concealed Features in a Military Environment," Analytical Science Corp. (TASC), Rept. TR-5859-1, Reading, MA, Nov. 1990.